

# Interstitial Doppler Optical Coherence Tomography as a Local Tumor Necrosis Predictor in Photodynamic Therapy of Prostatic Carcinoma: An *In vivo* Study

Beau A. Standish,<sup>1</sup> Kenneth K.C. Lee,<sup>2</sup> Xiao Jin,<sup>3</sup> Adrian Mariampillai,<sup>1</sup> Nigel R. Munce,<sup>1</sup> Michael F.G. Wood,<sup>1</sup> Brian C. Wilson,<sup>1,3</sup> I. Alex Vitkin,<sup>1,2,3</sup> and Victor X.D. Yang<sup>3,4,5</sup>

<sup>1</sup>Department of Medical Biophysics and <sup>2</sup>Radiation Oncology, University of Toronto, <sup>3</sup>Ontario Cancer Institute/University Health Network, <sup>4</sup>Department Electrical and Computer Engineering, Ryerson University, and <sup>5</sup>Imaging Research, Sunnybrook Health Sciences Center, Toronto, Canada

## Abstract

We have tested the feasibility of real-time localized blood flow measurements, obtained with interstitial (IS) Doppler optical coherence tomography (DOCT), to predict photodynamic therapy (PDT)-induced tumor necrosis deep within solid Dunning rat prostate tumors. IS-DOCT was used to quantify the PDT-induced microvascular shutdown rate in s.c. Dunning prostate tumors ( $n = 28$ ). Photofrin (12.5 mg/kg) was administered 20 to 24 hours before tumor irradiation, with 635 nm surface irradiance of 8 to 133 mWcm<sup>-2</sup> for 25 minutes. High frequency ultrasound and calipers were used to measure the thickness of the skin covering the tumor and the location of the echogenic IS probe within it. A two-layer Monte Carlo model was used to calculate subsurface fluence rates within the IS-DOCT region of interest (ROI). Treatment efficacy was estimated by percent tumor necrosis within the ROI, as quantified by H&E staining, and correlated to the measured microvascular shutdown rate during PDT treatment. IS-DOCT measured significant PDT-induced vascular shutdown within the ROI in all tumors. A strong relationship ( $R^2 = 0.723$ ) exists between the percent tumor necrosis at 24 hours posttreatment and the vascular shutdown rate: slower shutdown corresponded to higher treatment efficacy, i.e., more necrosis. Controls (needle + light, no drug,  $n = 3$ ) showed minimal microvascular changes or necrosis ( $4\% \pm 1\%$ ). This study has correlated a biological end point with a direct and localized measurement of PDT-induced microvascular changes, suggesting a potential clinical role of on-line, real-time microvascular monitoring for optimizing treatment efficacy in individual patients. [Cancer Res 2008;68(23):9987–95]

## Introduction

Photodynamic therapy (PDT) is an approved treatment for a variety of malignant diseases and has been used in clinical studies including brain, prostate, breast, pancreas, rectum, head and neck cancer, and Barrett's esophagus with dysplasia (1–6). Preclinical interstitial (IS) PDT studies have also been performed in parallel and include brain tumors (7), vertebral metastases (8), and prostate cancer (9).

Prostatic carcinoma remains a serious threat to men in the Western world, accounting for almost one quarter of all reported male cancers (10–12). Although incidence remains high, mortality rates have dropped over the last few decades due to improvements in screening and targeted treatment such as radiation therapy, radical prostatectomy, and hormonal therapies. Recent clinical trials have shown that IS PDT is a promising treatment modality for primary (13) and recurrent (14) prostate cancer. Some advantages of PDT include tumor selectivity, minimal invasiveness, and the ability to retreat safely and effectively.

PDT involves excitation of a photosensitizer in the presence of oxygen to produce highly reactive singlet oxygen, which is thought to be the main cytotoxic agent leading to cell death with most clinical and investigational photosensitizers (15). A requirement of prostate PDT in particular is to achieve adequate drug-light dose delivery to the entire prostate gland, while maintaining the integrity of surrounding tissues such as the urethra, bladder, rectum, and neurovascular bundle (16). Prostate cancer treatment techniques, including PDT, can lead to damage of these tissues, resulting in incontinence, proctitis, and/or sexual dysfunction. Real-time feedback based on the treatment-induced biological response would be ideal for monitoring and ensuring safety of these sensitive locations.

Optical technologies have been used to image and/or monitor blood flow in tumorous tissues (17, 18). Specifically, near-IR diffuse correlation spectroscopy (DCS), previously reported by Yu and colleagues (19), has been used to monitor tumor relative blood flow in bulk tumor tissue during PDT in an effort to predict treatment efficacy (tumor growth delay to 400 mm<sup>3</sup>). The authors observed that a decrease in the tumor (radiation-induced fibrosarcoma) vascular shutdown rate with Photofrin-PDT correlated with treatment efficacy ( $R^2 = 0.79$ ). Although this global vascular measurement system is suitable to monitor the average tumor response over an effective sampling volume of  $\sim 90$  mm<sup>3</sup>, the ability to provide real-time localized measurements of the vascular response with a spatial resolution suitable for monitoring both the prostate target boundary (to maximize efficacy) and/or sensitive tissues surrounding the prostate gland (to maximize safety) would be highly desirable. Our approach to achieve this is to use the real-time imaging by Doppler optical coherence tomography (DOCT), implemented with a minimally invasive sub-mm IS needle probe.

DOCT (20, 21) is an imaging modality that provides the functional extension of blood flow detection using an optical coherence tomography OCT (22) system. OCT is often considered as the optical analogue of high-frequency ultrasound imaging. Its advantages include the ability to image tissue structures at near histologic levels ( $<10$   $\mu$ m), while imaging blood flow within

**Requests for reprints:** Brian C. Wilson, Ontario Cancer Institute/University Health Network, Department of Medical Biophysics, University of Toronto, 610 University Avenue, Toronto, ON, Canada M5G 2M9. Phone: 416-946-4501, ext. 2952; Fax: 416-946-6529; E-mail: wilson@uhnres.utoronto.ca.

©2008 American Association for Cancer Research.  
doi:10.1158/0008-5472.CAN-08-1128

individual microvessels with velocities as low as 10 to 100  $\mu\text{m/s}$  (23–25). These real-time, noninvasive capabilities have been confirmed in subsurface blood flow detection in human skin (26), gastrointestinal tract (27), and retina (23, 28). Feasibility studies conducted by our and other groups showed the ability of DOCT to image the microvascular environment after exposure to vascular disrupting agents (29) and during single and two-photon PDT (9, 30–33).

In this study, a minimally invasive IS probe (0.7-mm diameter) was used in conjunction with a DOCT imaging system to overcome the imaging depth limitation of DOCT, which is typically 1 to 3 mm in nontransparent tissues, to gain access deep within prostate tumors (34). IS-DOCT continuously monitored and quantified the vascular response induced by Photofrin-mediated PDT in a Dunning rat prostate model. Images were acquired continuously pre-PDT, during, and post-PDT in real-time and analyzed to yield quantitative microvascular metrics. Individual tumors exhibited varying degrees of vascular shutdown, corresponding to different local light-fluence rates, as calculated by Monte Carlo simulations, within the imaging field of view of the probe. Potential relationships between the DOCT imaging metrics and the biological end point of percent tumor necrosis were investigated to test whether DOCT may be used as a predictor of tumor necrosis within the treated tissue.

## Materials and Methods

**Tumor model and PDT.** This study used 28 male Copenhagen rats (Charles River Laboratories) housed in standard conditions under a protocol approved by the Animal Care Committee of University Health Network, Toronto. Dunning prostate cells (Mat-Ly-Lu; American Type Culture Collection) were implanted intradermally in the right hind leg of all animals. The tumors were grown for 7 to 10 d to a diameter of 0.5 to 1 cm. Twenty-five rats were injected via the tail vein with 12.5 mg/kg of Photofrin (Axcan Pharma) 24 h before PDT treatment. Three control animals were used to measure the effects on the microvascular blood flow of the probe insertion and of the light irradiation [maximum fluence rate at IS probe depth ( $84 \text{ mWcm}^{-2}$ ) within the region of interest (ROI) of the IS needle: see below]. The tumor surface was irradiated superficially through the intact skin, for 25 min, with a 635 nm broad beam diode laser (Laboratory of Applied Biophotonics, University Health Network) collimated to a 1-cm diameter spot size. The optical power was measured before each treatment with a calibrated optical power meter (840-C; Newport Instruments, Canada) to achieve different surface irradiance ( $\text{mWcm}^{-2}$ ). The animals were chosen at random to populate 5 different irradiance groups (8, 16, 33, 66, and  $133 \text{ mWcm}^{-2}$ ). Before PDT, the animals were anaesthetized with oxygen and 2% isoflurane through a nose cone. The tumor surface was prepared by depilation by shaving and application of Nair (Church & Dwight Canada Corp.). The rats were kept at body temperature ( $37^\circ\text{C}$ ) during all procedures using a heating pad. At 24 h post-PDT, the animals were euthanized by intracardiac injection of euthanyl (0.5 mL) and the tumors were excised intact for histology.

**DOCT system, IS probe, and high frequency ultrasound imaging.** A detailed description of the time-domain DOCT system and IS needle probe has been given previously (9, 35). Briefly, the 8 kHz system uses a near-IR source at 1.3  $\mu\text{m}$  center wavelength, with a coherence length of  $\sim 10 \mu\text{m}$  in tissue, and Doppler flow sensitivity of  $\sim 20 \mu\text{m/s}$ . The IS-DOCT needle probe is composed of a single-mode optical fiber fusion spliced to a lens that focuses the light into the tissue. These components are encased in a transparent catheter (outer diameter, 0.4 mm) and threaded into a 22G echogenic needle (outer diameter, 0.7 mm), and actuated by a linear scanner. The probe is driven over 1 mm along the length of the enclosing catheter and combined with the coherence depth scanning to generate a two-dimensional DOCT image (1 mm lateral by 1 mm depth).

Structural and color Doppler images were continuously acquired at a rate of 1 frame per second (fps) and subdivided into 3 imaging time points: before ( $t = 0\text{--}10 \text{ min}$ ), during ( $t = 10\text{--}35 \text{ min}$ ), and post ( $t = 35\text{--}45 \text{ min}$ ) PDT treatment. Regions of flow were color coded in the Doppler images. Detected Doppler signals represent regions of flow within the vasculature. The Doppler background artifact due to bulk tissue motion was minimized by first processing the color-Doppler images with a histogram rejection algorithm (36). A Doppler threshold based on the mean Doppler signal from a region of stationary tissue was used to further separate blood flow detection from background noise. Blood flow velocities were not calculated, as the geometry of the Doppler angles with various vessels was not known *a priori*. The Doppler signals were used as a binary metric to measure flow versus no-flow regions. Cross-sectional areas were then quantified by summing Doppler-positive pixel counts. The results were averaged into 1-min interval bins and defined as the vascular index (VI; ref. 32).

High frequency ultrasound (HFUS) images (Vevo770; Ultrasonics) were taken with a 40 MHz transducer at 17 fps to determine the location of the IS probe and the global tissue architecture, as seen in Fig. 1A. The IS probe was inserted toward the bottom margin of the tumor with the imaging direction upwards towards the tumor bulk (Fig. 1A). The HFUS images were used (Fig. 1B to C) to measure the depth of the IS-DOCT probe and the thickness of the overlying skin for use in Monte Carlo simulations.

**Tissue properties and Monte Carlo modeling.** The optical absorption ( $\mu_a$ ) and reduced scattering ( $\mu_s'$ ) coefficients of rat prostate tumor were calculated by measuring the diffuse reflectance and transmittance using an integrating sphere setup and Monte Carlo modeling of light transport (37). A white light broadband (300–800 nm) mercury/xenon lamp (Spectral Energy) and collimating optics were used to illuminate the sample. The transmitted and reflected spectra were recorded as a function of wavelength (333–1,111 nm) with 2 15-cm diameter integrating spheres (SphereOptics) coupled to a portable spectrometer (SD2000; Ocean Optics). Although a wide range of spectral data were acquired, only pertinent  $\mu_a$  and  $\mu_s'$  values were calculated that corresponded to the central wavelength of the PDT laser (635 nm). Upon excision,  $\sim 5 \text{ min}$  after euthanasia, the rat prostate tissue was directly placed into the reflectance/transmittance (R/T) integrating setup. The sample was inserted between two coverslips, where the tumor sample was  $\sim 1 \text{ mm}$  thick (1 cm diameter). The R/T interrogation region was  $\sim 4 \text{ mm}$  (diameter). Three different measurement locations in freshly excised rat tissue were averaged and used to determine  $\mu_a$  and  $\mu_s'$ , applying an inverse calculation based on Monte Carlo-generated look-up tables (38). These tissue coefficients were used in conjunction with published optical properties for the rat dermis (39) in a two-layer Monte Carlo simulation with a collimated surface irradiance for a 1-cm beam diameter (40). The two-layer Monte Carlo simulation modeled the shape of an ellipse to account for the curvature of the tumor surface, and used  $10^8$  photons to provide a statistically significant number of interactions yielding an accurate fluence rate estimate as a function of depth. These values were then scaled to the experimentally measured surface irradiance, resulting in the fluence rate (at depth) of the IS probe. The dermis thickness ( $\Delta x_2$  in Fig. 1B) was measured to be  $0.6 \pm 0.1 \text{ mm}$  from the HFUS images, and the IS probe placement ( $\Delta x_1$  in Fig. 1B) ranged from 2 to 8 mm.

**Histology.** The intradermal prostate tumors were excised 24 h post-PDT and stored in 10% formalin solution. H&E staining was used to identify treatment-induced tumor necrosis. Four-micrometer-thick tissue sections were digitized with a bright-field whole-slide scanner (Scanscope CS; Aperio Technologies), and the resulting images were analyzed with Aperio ImageScope v.8.0 software. The localization of the IS-DOCT ROI within the histologic sections was accomplished as follows. HFUS images were obtained with the IS needle in place, providing the location of the upper edge of the IS needle within the tumor (Fig. 2A, *black dotted line*). The exact lateral position of the DOCT ROI within the tumor was not determined during imaging, as we did not tattoo or physically mark the position to avoid affecting histologic results. Therefore, the percent necrosis was an average value of the whole lateral region at depth (Fig. 2A, *white box*). The

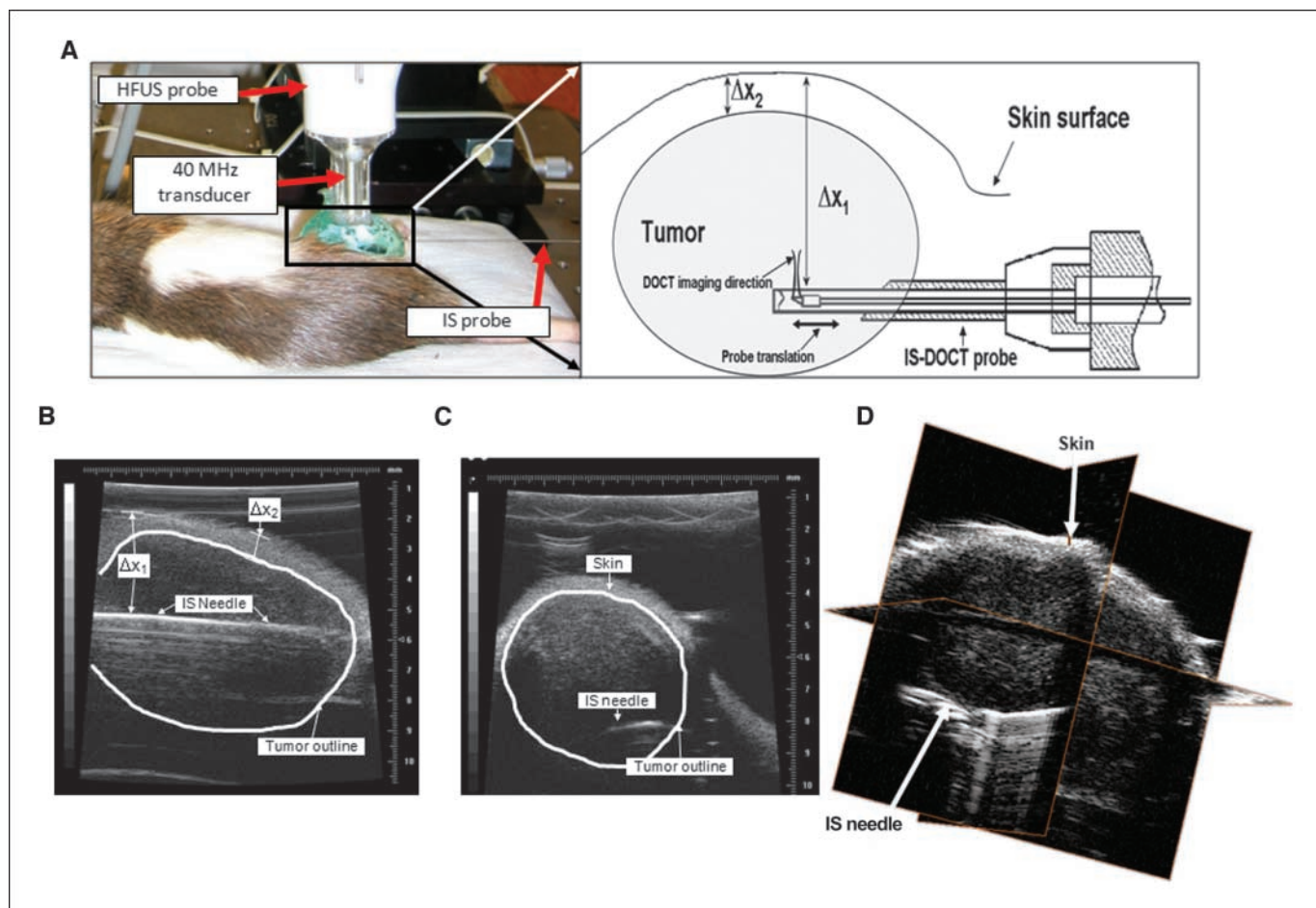


**Figure 1.** A, the experimental set up showing the external HFUS probe and IS-DOCT probe inserted near the base of the tumor. Magnified box, geometry of IS-DOCT measurements: the skin thickness ( $\Delta x_2$ ,  $0.6 \pm 0.1$  mm) and depth of IS probe ( $\Delta x_1$ , 2–8 mm), as measured by HFUS were used in Monte Carlo simulations of fluence rates in the IS-DOCT ROI. B, HFUS side view location of the IS probe in tumor mass. C, corresponding end-on view. D, 3-D visualization. The major vertical and horizontal scales are in 1-mm increments. White outlines represent tumor borders (B and C).

H&E tumor regions were analyzed by counting the total number of positive pixels in the H&E-stained sections (*pink*). In the H&E sections, a positive pixel count represented a loss of nuclear integrity when compared with a negative count (*purple*), where the nucleus was still intact. Using these

markers, a mask was created highlighting the respective positive pixel counts, and defined the percent necrosis (Fig. 2B) in the ROI as a ratio of the mask area (positive pixel counts) to the remaining area (negative pixel counts) within the ROI.

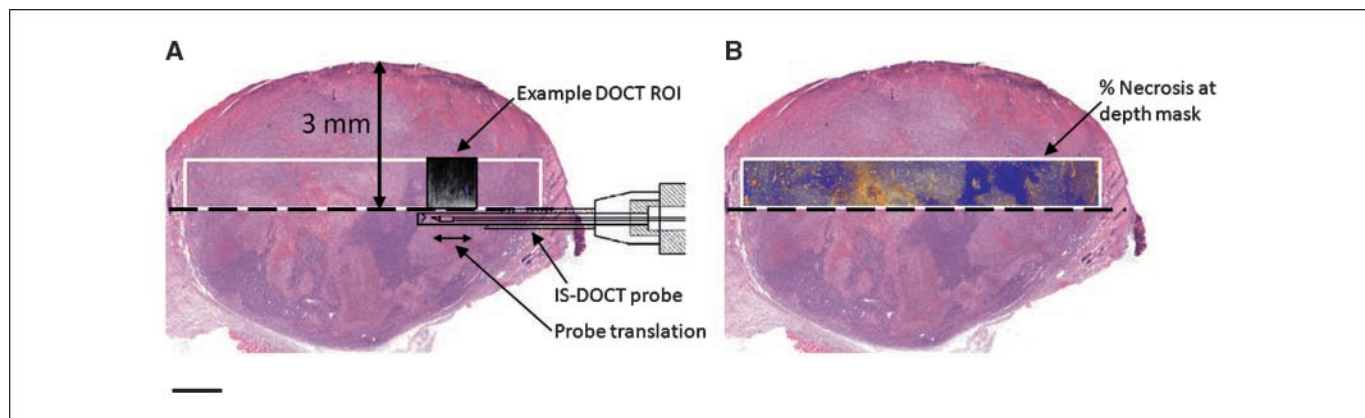


**Figure 2.** Example of necrosis assessment in H&E histology. A, H&E-stained slide with IS-DOCT ROI (black box) at an IS needle depth of 3 mm. Dashed black line, upper edge of needle probe. B, imaging mask based on necrotic or nonnecrotic tissue. Orange sections of the mask outline necrotic tissue areas (positive pixel counts), whereas blue sections represent the nonnecrotic tissue (negative pixel counts). Percent necrosis was defined as a ratio of the orange to the total areas. Scale bar, 1 mm.

## Results

Xenograft tumors were successfully grown in all 28 rats, with average dimensions of  $1.0 \pm 0.2 \text{ cm} \times 0.8 \pm 0.2 \text{ cm} \times 0.5 \pm 0.1 \text{ cm}$  ( $L \times W \times H$ ) as measured by calipers and HFUS. Immediately after treatment, PDT responses, including erythema and edema, were observed in all 25 rats undergoing PDT treatment. These responses were not observed in the three control animals. No treatment-induced deaths occurred.

The  $\mu_a$  and  $\mu_s'$  values, at the PDT treatment wavelength of 635 nm, derived from RT (R/T) spectral measurements are shown in Fig. 3, yielded values of  $0.77$  and  $7.55 \text{ cm}^{-1}$ , respectively. As an example, Fig. 3C shows the resulting fluence rate-depth distribution from the two-layer Monte Carlo simulation for an incident ( $84 \text{ mWcm}^{-2}$ ) 1-cm diameter beam. In highly scattering medium, the fluence within the first 2 mm may be 3 to 4 times higher than the incident beam irradiance (41). This build-up was observed (Fig. 3D) in our model and is due to multiple scattering and the optical property mismatches at the air/skin and skin/tumor boundaries.

The IS-DOCT system continuously acquired, processed and displayed structural and blood flow data before (0–10 min), during (10–35 min), and post-PDT (35–45 min) treatment in all animals. Figure 4A shows an imaging sequence representing every 5th minute of imaging for a PDT treatment of  $32 \text{ mWcm}^{-2}$ . The color-Doppler functional information was overlaid onto the structural OCT images with the measured Doppler frequency shift being proportional to the velocity of the moving blood (These and all subsequent light variables correspond to the IS probe location). When the velocity of the blood is greater than  $\pm F_a/2$ , where  $F_a$  is the scan rate of the OCT system (8 kHz), aliasing of the detected signal occurs. This is shown by the insert of the 0 min time point in

Fig. 4A, where the Doppler signal wraps from the negative (*red*) to positive frequencies (*blue*), representing high velocity blood. Counter-propagating blood flow occurs when the IS-DOCT image plane intersects both arteries and veins. This was observed in Fig. 4A at the 10-minute time point, where the insert shows an artery/vein pair represented by the solid blue and red color-coded regions. Note that these subtleties have a minimal influence on the VI metric, as it depends on cross-sectional area of detected vasculature and not the absolute blood flow velocities.

The number of vessels detected in the DOCT field-of-view varied between animals from 2 to 11 in the  $1 \times 1 \text{ mm}$  field of view, with minimum and maximum detected diameters of the vessels of  $\sim 30$  and  $\sim 270 \mu\text{m}$ , respectively. Minor lateral drifting ( $<150 \mu\text{m}$ ) occurred in the OCT structural images during parts of the 45-minute imaging sessions and was probably due to tissue motion caused by the animal breathing. The structural OCT images in the tumors typically showed few distinct features, whereas normal tissue structures, such as boundaries between skin and muscle and between muscle layers, were clearly visualized.

In each tumor the VI was calculated by pixel summing the color-Doppler sequences during the imaging session, where minimum and maximum interanimal VI counts were 151 and 2,045, respectively (total number of pixels, 90 000 per frame). An illustrative vascular response curve is presented in Fig. 4B. All PDT animals exhibited a slight increase in the VI value upon insertion of the IS probe and at the beginning of treatment, followed by varying degrees of the PDT-induced vascular shutdown (40–100%). It was common to observe small fluctuations in the VI throughout the PDT treatment. The PDT-induced vascular shutdown rate during light exposure was then characterized by the ratio of the total decrease in VI ( $VI_{\text{max}} - VI_{\text{min}}$ ) to the time

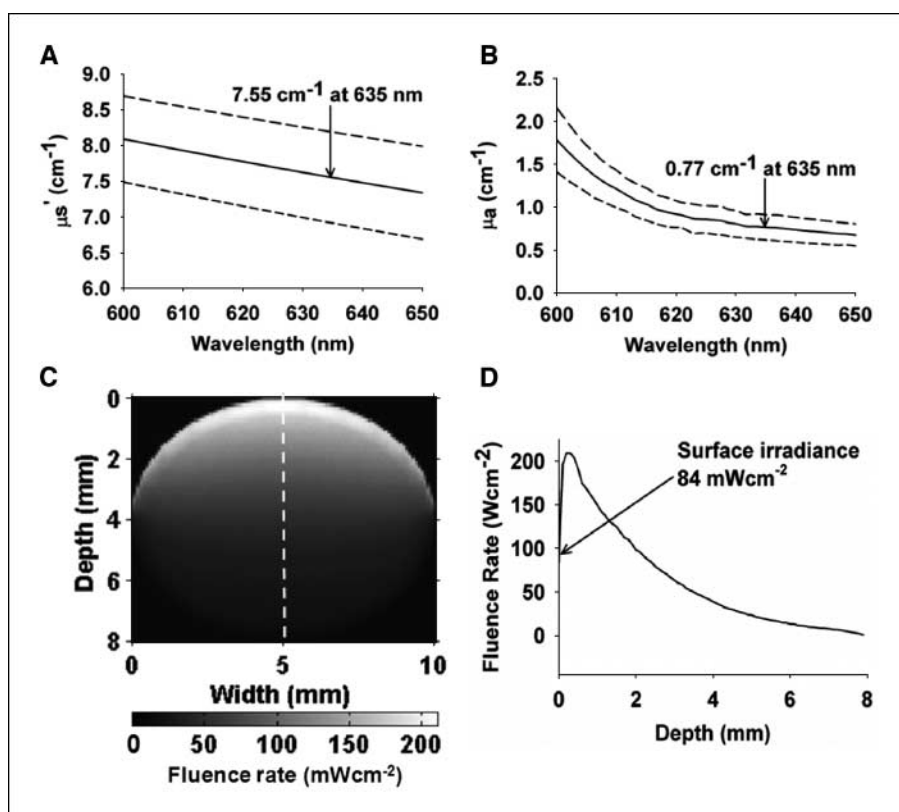


**Figure 3.** A, reduced scattering spectra for prostate tumor tissue. B, corresponding absorption spectra. Dashed lines, SEs in the measurement (A and B). C, fluence rate as a function of depth ( $84 \text{ mWcm}^{-2}$  surface irradiance) produced by a  $10^8$  photon, two-layer (ellipse) Monte Carlo model with a 1-cm-diameter incident beam. Dashed vertical line, region used in D, for fluence rates as a function of depth through center of tumor.

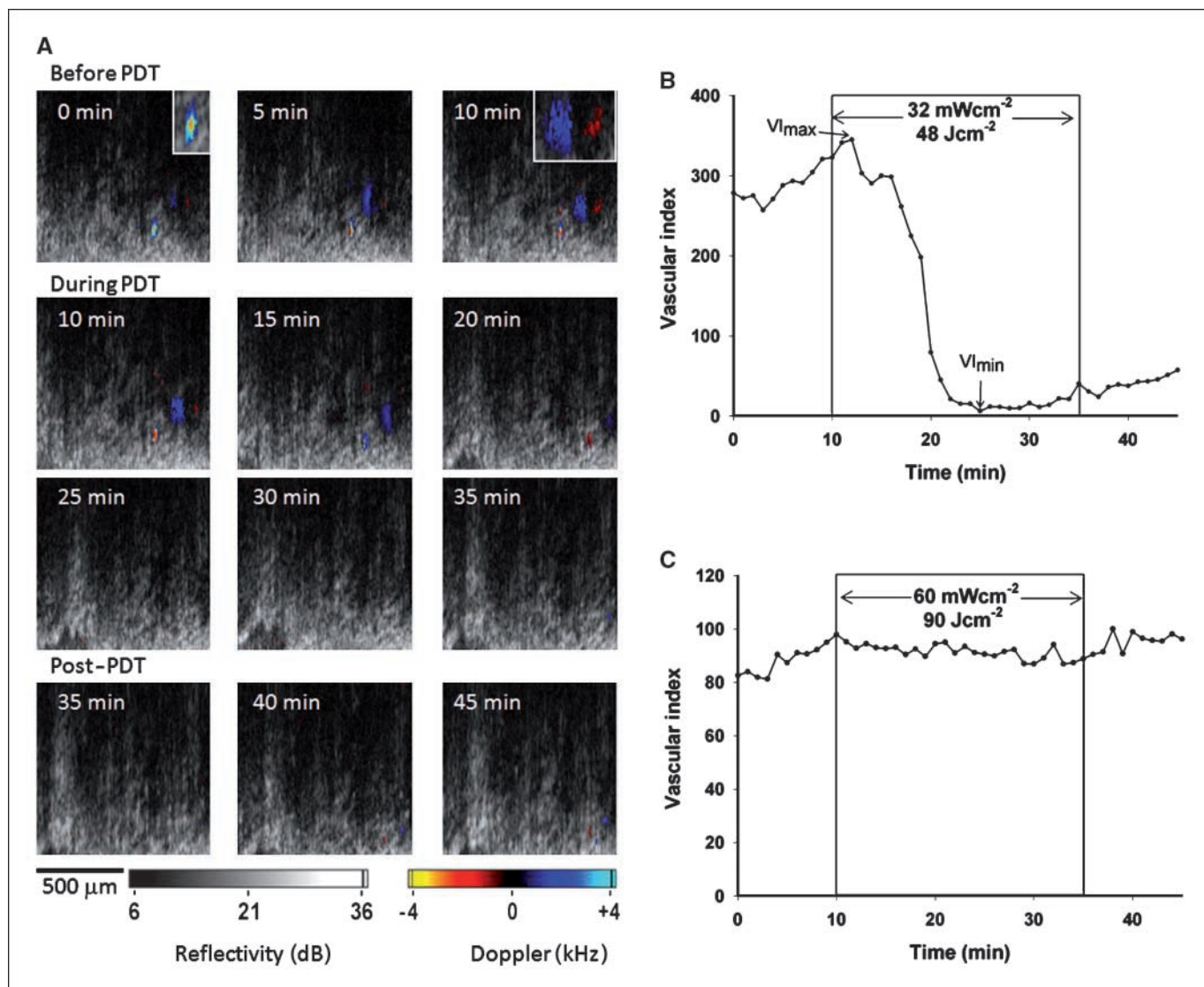


**Figure 4.** A, IS-DOCT imaging sequence of color-Doppler blood flow detection overlaid onto structural OCT images before, during, and post-PDT treatment. The inserts are  $\times 2$  magnifications showing aliasing (0 min) and counter-propagating flows (10 min). B, vascular index as a function of time in a single animal showing the vascular shutdown during PDT light exposure and the definitions of  $V_{\text{max}}$  and  $V_{\text{min}}$ . C, control animal (light, no photosensitizer). Fluence rates and fluence listed in B and C are values at the depth of the IS-DOCT probe.

( $T_{\text{max}} - T_{\text{min}}$ ) taken to achieve this:  $V_{\text{max}}$  and  $V_{\text{min}}$  were defined as the maximum and minimum values during treatment. The controls also experienced a minor increase in the VI upon probe insertion, but there were no significant systematic changes throughout exposure to light in the absence of photosensitizer (Fig. 4C).

Twenty-four hours post-PDT, tumors were excised, stained with H&E, and the percent necrosis was quantified within the IS-DOCT ROI. Necrosis in the dermis and tumor core was observed in one of the control animals (Fig. 5). In that particular case, there was evidence of a small surface lesion in the region of the tumor, which may have been caused by scratching and/or biting of the irritated xenograft region. For the PDT group, as the subsurface fluence rate was increased from  $\sim 6$  to  $\sim 36 \text{ mWcm}^{-2}$ , the percent necrosis within the IS-DOCT ROI reached a maximum. At higher fluence rates, up to the maximum of  $84 \text{ mWcm}^{-2}$ , the percent necrosis then decreased (Fig. 5).

Figure 6A summarizes the percent tumor necrosis, determined from the H&E-stained sections, as a function of the subsurface fluence rate ( $\text{mWcm}^{-2}$ ). The biological response at higher fluence rates ( $>60 \text{ mWcm}^{-2}$ ) resulted in  $<11\%$  necrosis within the ROI. Busch and colleagues (42) reported that higher fluence rates ( $>75 \text{ mWcm}^{-2}$ ) in Photofrin-mediated PDT resulted in the development of significant gradients in tumor hypoxia as one moves away from a perfused blood vessel. This lack of oxygen will limit the photochemical reaction, resulting in a poor biological response. Our data also suggests that lower fluence rates ( $<18 \text{ mWcm}^{-2}$ ) resulted in a reduced biological response, where  $<21\%$  tumor necrosis was observed. The intermediate fluence rates ( $21\text{--}60 \text{ mWcm}^{-2}$ ) produced the highest level of necrosis ( $34\text{--}41\%$ ), with the maximum occurring at  $36 \text{ mWcm}^{-2}$ . The control animals (IS probe, light, no drug) showed an average tumor necrosis of  $4\% \pm 1\%$  at the control irradiance of  $133 \text{ mWcm}^{-2}$ .

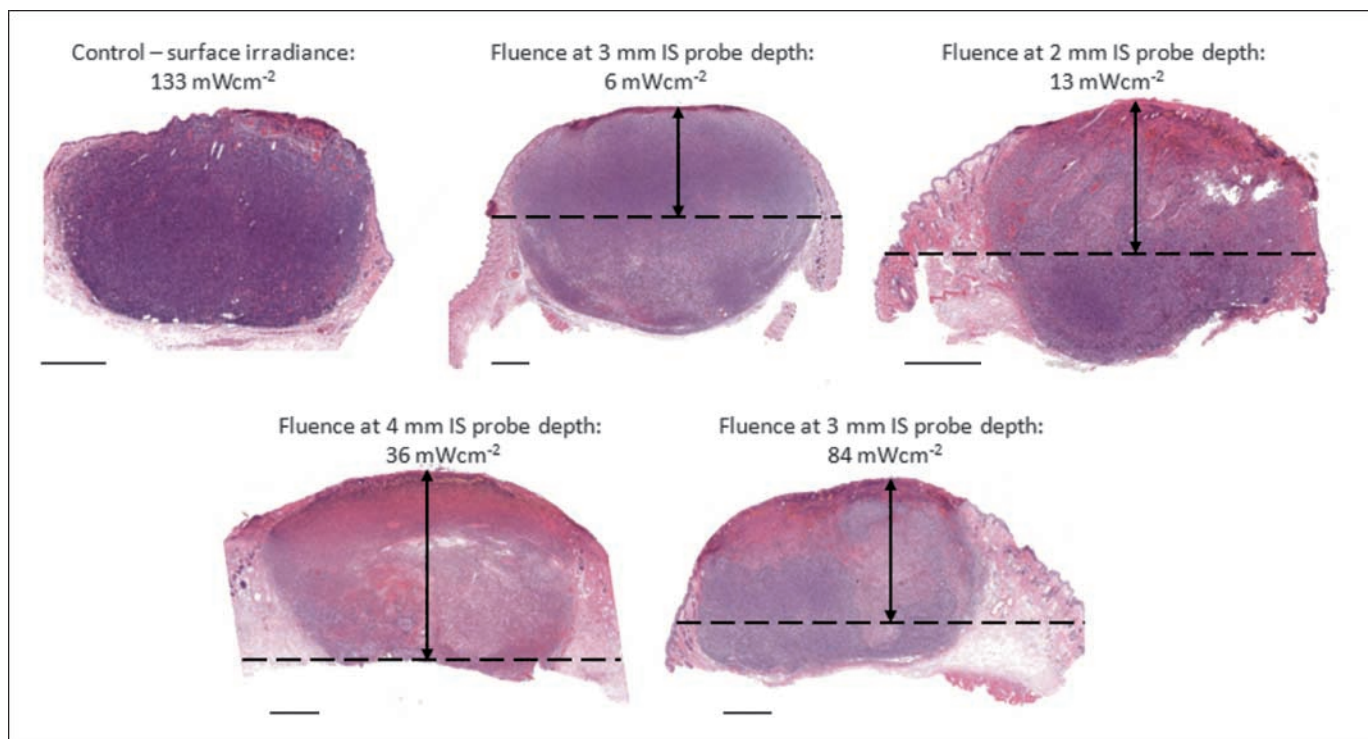


**Figure 5.** H&E histology in different PDT-treated and control tumors. Horizontal dashed line, the upper edge of the IS-DOCT probe. Scale bar, 1 mm.

The VI data were split into four groups, as shown in Table 1. Two groups were based on the IS probe location of inside or outside the PDT-induced necrotic region, and two groups were based on the % change in the measured VI. A cutoff value of 20% change in the VI was chosen for each tumor, as this corresponded to the maximum observed VI change (control group) due to insertion of the probe and exposure to light. This organization of the data was enabled by the HFUS and histologic correlation.

The relationship between the percent tumor necrosis and the flow reduction rate is displayed in Fig. 6B for all subgroups and the

controls. Here, the flow reduction rate is defined as the percent decrease per minute in the VI value in each tumor during the PDT treatment interval. For regression analysis, the groups were separated into two sets. Those animals in which the IS-DOCT probe was located within the necrotic region (subgroup A,  $n = 9$ ) were the most relevant to assessing the ability of DOCT to predict the biological end point and were, therefore, separated from the remaining subgroups B to D.

Within subgroup A, a marked and statistically significant decrease in PDT treatment efficacy was observed when there was

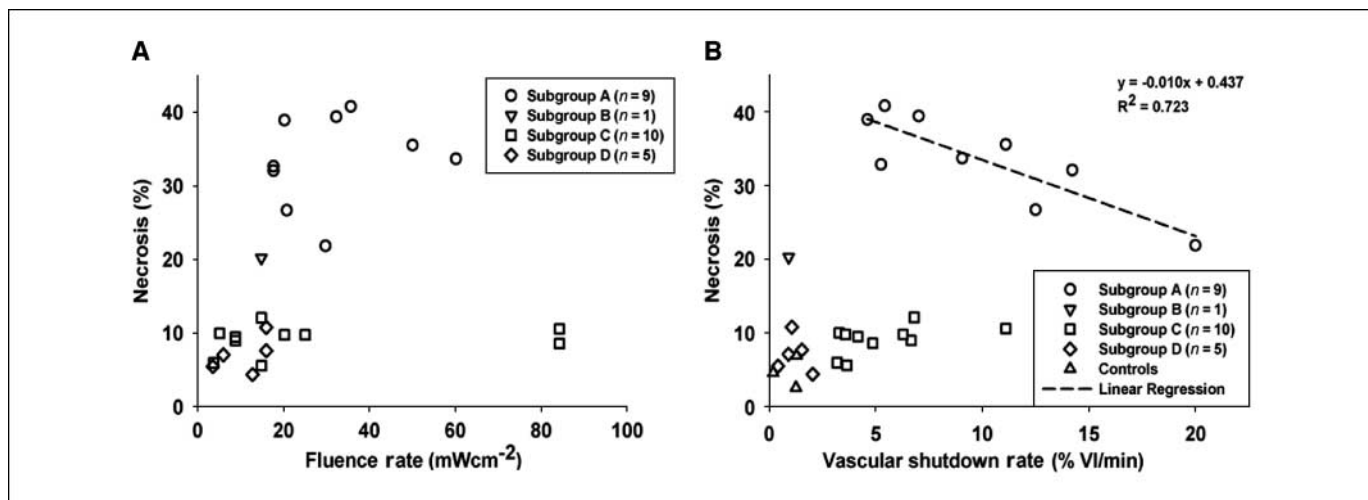


**Figure 6.** A, PDT-induced tumor necrosis as a function of the light fluence rate (4–84 mWcm<sup>-2</sup>) for individual tumors. B, correlation between percent tumor necrosis and flow reduction rate of all subgroups. Within subgroup A, a marked and statistically significant ( $R^2 = 0.723$ ) decrease in PDT treatment efficacy was observed when there was an increased rate of vascular shutdown.

**Table 1.** Number of tumors in each subgroup

DOCT response	Probe within necrotic region	Probe outside necrotic region
>20% shutdown in VI	A. <i>n</i> = 9	C. <i>n</i> = 10
<20% shutdown in VI	B. <i>n</i> = 1	D. <i>n</i> = 5

an increased rate of vascular shutdown. The highest percent necrosis (32–41%) occurred when the VI decreased at a rate of 5% to 10% per minute. The relationship between the percent necrosis and vascular shutdown rate was not known *a priori*, so a simple linear fit was applied, yielding  $R^2 = 0.723$ .

Subgroups B to D showed significant changes in the vascularity (up to ~11% per minute) but did not strongly correlate with the percent necrosis (<20%). Hence, even outside the necrotic region, significant changes in the vascular response were observed. This can be interpreted two ways. If the probe was inserted outside a region of necrosis (as predicted *a priori*, for example by Monte Carlo modeling), the VI may be indicative of potential downstream PDT effects, such as a feeder vessel thrombosis. The thrombosis may temporarily cut off blood supply to a region, then dislodge, causing significant changes in the VI, which are not directly related to the local PDT treatment. Alternatively, if the probe is placed within a region of expected necrosis (again, as potentially estimated by Monte Carlo modeling), the VI is indeed a predictor of the local tumor response. Future work is required to include further posttreatment monitoring to determine if these vascular effects, as measured by DOCT, are temporary or permanent.

## Discussion

Given the complex interplay of contributing factors in PDT, a real-time feedback method that can be used during PDT treatment delivery and that can predict the likely tissue response is critical to “individualize” treatments for maximum efficacy. Current approaches to this include fiber optic detectors to monitor the changes in light transmission (43), photosensitizer pharmacokinetics (44), tissue optical properties (45), tumor oxygenation (46–48), and blood flow monitoring (9, 49, 50). All such studies have illustrated the heterogeneity of PDT responses. In the present study, we have shown the integration of several different technologies (HFUS, Monte Carlo modeling, and IS-DOCT) to monitor PDT-induced vascular changes in real-time in a minimally invasive fashion. A strong relationship between the IS-DOCT vascular imaging metric of blood flow reduction rate and the biological end point of tumor necrosis was determined. Although this is a relatively early-stage response metric (24 hours posttreatment), it is likely that this would relate to other clinically relevant metrics such as tumor growth delay and/or cure rates (51).

We characterized the change in the cross-sectional vascular area as a function of PDT treatment time to yield the imaging metric of vascular shutdown rate. The vascular shutdown rate varied in the animal population according to the fluence rate in the IS-DOCT imaging ROI. Deeper IS probe placements resulted in lower fluence rates as calculated by Monte Carlo simulations. After the insertion of the IS probe into the tumor, the VI continued to increase (<20%) for the first few minutes before leveling off. This was observed in all animals, including controls, and may be a result of reperfusion after

transient pressure and/or vasodilation in the detected vessels due to local trauma from the needle insertion. Further miniaturization of the IS probe should minimize this effect. Upon light exposure, a small (<10%) increase in the VI was observed, followed by a rapid decrease in the PDT-treated tumors. Yu and colleagues (19) reported similar trends in the PDT-induced vascular response of radiation-induced fibrosarcoma tumors with DCS, although the initial increase in blood flow was much higher (>50%). This difference may be due to the fact that IS-DOCT monitors individual (micro)vessel changes, whereas DCS measures a global, tissue-average vascular response. These authors also suggested that the initial increase in the tumors is due to arterial vasodilatation of normal tissue, in response to initial tumor hypoxia due to photochemical consumption of oxygen. We observed small ( $\pm 10\%$  of total VI) fluctuations, which seems to be random, in the VI values throughout the DOCT imaging sessions, likely due in part to the changing tumor environment during PDT; small fluctuations ( $\pm 10\%$  of total VI) were also seen in the controls animals, probably due to the presence of the IS probe. One animal showed <20% change in the VI, yet the IS probe was within a tumor region that became necrotic (subgroup B). In this apparent “outlier,” it is possible that the IS needle injured a tumor feeder vessel, resulting in local necrosis. Further work is required to determine if this is a serious source of measurement artifact.

The observed vascular response (within and outside necrotic region) is of particular relevance to the potential of DOCT as a real-time feedback technique during PDT. For example, if the probe is in a region of tissue where a marked PDT effect is achievable, then the extent of this effect may be related to the rate of vascular shutdown as monitored by DOCT. However, at the present time, it is not clear why a vascular response was also observed outside the necrotic region; the thrombosis/hemorrhage scenario affecting out-of-treatment downstream regions need further corroboration.

It is possible that these effects may be due to measurement artifacts, such as a change in the IS pressure or direct mechanical disruption of a feeder vessel. However, this situation is not likely because the control animals exhibited minimal changes in the VI upon probe insertion and exposure to light (no photosensitizer). This leaves the possibility of a transient vascular response occurring through the creation and dislodging of vascular thrombi (52) and/or a subnecrotic PDT-induced vascular response, as alluded to above. We plan to use the mouse window chamber model (53) to limit possible vascular artifacts from the IS probe, while obtaining direct visualization of the PDT-induced vascular response via DOCT. In addition to suggesting further scientific investigations of the underlying vascular mechanisms in PDT, it thus remains to be seen if IS-DOCT can be used as a stand-alone treatment monitoring/predictive outcome. In this regard, the technique seems to display a high sensitivity for eventual necrosis, but relatively poor specificity, at least in this tumor model, which could lead to overestimation of the extent of tissue damage induced by PDT.

An attractive feature of IS-DOCT is the ability to monitor the localized vascular response to treatment in deeply situated tissues such as, for example, the boundary between the prostate and rectal wall. Despite the changes in the vascular response measured in regions that did not become necrotic, clinical value remains in the observation that a minimal change in the vascular shutdown (controls or treatment animals) corresponded to a negligible tumor necrosis. Hence, even if the specificity remains low in the clinical setting, IS-DOCT could be used to monitor sensitive normal tissue

regions (e.g., the rectum in the case of prostate treatments), based on observing continuous blood flow to ensure no damage.

The relationship between the vascular shutdown rate and tumor necrosis ( $R^2 = 0.723$ ) in the PDT-treated animals suggests that DOCT may be used to predict localized necrosis. A study in canine sarcoma, treated by radiation therapy, indicates that 70% to 80% necrosis is required for successful local control (no evidence of tumor recurrence in canines living with leg for at least 6 months; ref. 50). Such levels were achieved only in the superficial regions of tumor in the present model. For example, the top 1.7 mm of tumor in Fig. 5D showed 71% necrosis, whereas there was only 41% necrosis within the corresponding IS-DOCT ROI (at 5 mm depth). Hence, we were likely undertreating the tumors at the IS-DOCT depth. At the same time, this also shows the potential value of the IS-DOCT technique because, if the predictive relationship between the DOCT metric(s) and the probability of local necrosis can be determined, then treatment could have been continued to achieve higher response at the depth of interest (e.g., the tumor base). In addition, considerable variability was observed in the tumor responses (% necrosis) with similar PDT treatments, highlighting the intrinsic heterogeneity of the biological response to PDT, and emphasizing the need for individualized treatment monitoring and optimization.

A generic drawback of OCT is the limited imaging depth in most biological tissues (~1–3 mm). Previously, this restricted OCT imaging to luminal surfaces, epithelial layers, transparent organs, skin, and surgically exposed surfaces. With the advent of the IS probe technology (diameter, 0.7 mm), deeply seated tissues can be imaged, providing localized measurements. However, with our current imaging technique, the exact lateral position of the DOCT ROI within the tumor is not known. To improve the localization of the DOCT ROI in future studies, a marked thread may be inserted alongside the IS probe, via a two-channel catheter. Upon removal of the probe, the thread will remain in place and be included in the sectioning of histology, allowing for a more accurate localization of the IS probe during imaging.

The IS-DOCT system may provide local monitoring of treatment responses in deeply situated tissues, such as at tumor boundaries and critical normal tissues. In many cases, this will require simultaneous (continuous) monitoring by several probes, for which a multichannel instrument is required. Such a system is under development and a similar system has been recently reported by Yuan and colleagues (54). Furthermore, a larger tissue region may be monitored using a three-dimensional rotary pullback probe (55), increasing the interrogation region from ~1 mm<sup>2</sup> to >300 mm<sup>3</sup> (1.5 mm radius; 50 mm pull back). This will be of particular value in

monitoring the PDT responses in endoscopic sites such as Barrett's esophagus (56).

In conclusion, we have shown the ability of DOCT to monitor and quantify in real-time the PDT-induced vascular changes at locations deep within solid tumors via a minimally invasive IS imaging probe. Measurements (HFUS) of the probe depth and overlying skin thickness allowed calculation of the fluence rate delivered within the IS-DOCT ROI. This provided a direct correlation of the local PDT biological response (histologically derived necrosis) with an objective measure of the corresponding local microvascular response. This technique may prove useful in monitoring critical boundary regions within and surrounding target tumor tissue, such as in the prostate, during PDT treatments. We envision combining this approach with previously reported PDT dosimetric measurements, such as tissue optical properties and/or tumor oxygenation, to provide optimized and individualized treatment that takes into account the intrinsic heterogeneity of tissues and their complex PDT response. Thus, for example, ongoing clinical trials at this institution indicate that PDT salvage therapy in locally recurrent prostate cancer after radical radiotherapy is safe and well-tolerated, but that the interpatient and inpatient extent and completeness of PDT-induced necrosis are highly variable (5). The current technique incorporates preplanning of IS cylindrical diffusing fiber source placement, transrectal ultrasound guidance for IS fiber placement, and posttreatment (7 days) assessment of the zones of PDT-induced avascularity using contrast-enhanced magnetic resonance imaging. Addition of IS-DOCT to this platform will allow on-line adjustment of treatment, and this will be a primary focus of continuing studies and translation to the clinic. This work will be accomplished in parallel with the use of DOCT for monitoring responses during endoscopic PDT (32).

## Disclosure of Potential Conflicts of Interest

No potential conflicts of interest were disclosed.

## Acknowledgments

Received 3/26/2008; revised 8/28/2008; accepted 9/24/2008.

**Grant support:** Canadian Cancer Society through a grant from the National Cancer Institute of Canada. The Canadian Institutes of Health Research, the OCE Centre for Photonics, the Premier's Research Excellence Award, the Gordon Lang and the Samuel B. McLaughlin Foundations supported the development of the IS-DOCT system.

The costs of publication of this article were defrayed in part by the payment of page charges. This article must therefore be hereby marked *advertisement* in accordance with 18 U.S.C. Section 1734 solely to indicate this fact.

We thank Mathieu Roy and Dr. Robert Weersink for the assistance with the Monte Carlo and tissue property modeling, and Dr. Allison Brown for providing expertise in HFUS.

## References

- Overholt BF, Wang KK, Burdick JS, et al. Five-year efficacy and safety of photodynamic therapy with Photofrin in Barrett's high-grade dysplasia. *Gastrointest Endosc* 2007;66:460–8.
- Lou PJ, Jones L, Hopper C. Clinical outcomes of photodynamic therapy for head-and-neck cancer. *Technol Cancer Res Treat* 2003;2:311–7.
- Huang Z. A review of progress in clinical photodynamic therapy. *Technol Cancer Res Treat* 2005;4:283–93.
- Wolfsen HC. Uses of photodynamic therapy in premalignant and malignant lesions of the gastrointestinal tract beyond the esophagus. *J Clin Gastroenterol* 2005;39:653–64.
- Trachtenberg J, Bogaards A, Weersink RA, et al. Vascular targeted photodynamic therapy with palladium-bacteriopheophorbide photosensitizer for recurrent prostate cancer following definitive radiation therapy: assessment of safety and treatment response. *J Urol* 2007;178:1974–9.
- Szeimies RM, Morton CA, Sidoroff A, Braathen LR. Photodynamic therapy for non-melanoma skin cancer. *Acta Dermatol Venereologica* 2005;85:483–90.
- Muller PJ, Wilson BC. Photodynamic therapy of brain tumors - a work in progress. *Lasers Surg Med* 2006;38:384–9.
- Akens MK, Yee AJM, Wilson BC, et al. Photodynamic therapy of vertebral metastases: evaluating tumor-to-neural tissue uptake of BPD-MA and ALA-PpIX in a murine model of metastatic human breast carcinoma. *Photochem Photobiol* 2007;83:1034–9.
- Standish BA, Jin X, Smolen J, et al. Interstitial Doppler optical coherence tomography monitors microvascular changes during photodynamic therapy in a Dunning prostate model under varying treatment conditions. *J Biomed Opt* 2007;12:034022.
- Jemal A, Siegel R, Ward E, Murray T, Xu J, Thun MJ. Cancer statistics, 2007. *CA Cancer J Clin* 2007;57:43–66.
- Canadian Cancer Society/National Cancer Institute

- of Canada: Canadian Cancer Statistics 2007. Toronto: Canadian Cancer Society/National Cancer Institute of Canada; 2007. p. 4.
12. CancerStats Incidence - UK. London: Cancer Research UK; 2006. p. 2.
  13. Du KL, Mick R, Busch TM, et al. Preliminary results of interstitial motexafin lutetium-mediated PDT for prostate cancer. *Lasers Surg Med* 2006;38:427-34.
  14. Nathan TR, Whitelaw DE, Chang SC, et al. Photodynamic therapy for prostate cancer recurrence after radiotherapy: a phase I study. *J Urol* 2002;168:1427-32.
  15. Weishaupt KR, Gomer CJ, Dougherty TJ. Identification of singlet oxygen as the cytotoxic agent in photo inactivation of a murine tumor. *Cancer Res* 1976;36:2326-9.
  16. Huang Z, Chen Q, Dole KC, et al. The effect of Tookad-mediated photodynamic ablation of the prostate gland on adjacent tissues - *in vivo* study in a canine model. *Photochem Photobiol Sci* 2007;6:1318-24.
  17. Sunar U, Makonnen S, Zhou C, et al. Hemodynamic responses to antivasular therapy and ionizing radiation assessed by diffuse optical spectroscopies. *Optics Exp* 2007;15:15507-16.
  18. Zhou C, Choe R, Shah N, et al. Diffuse optical monitoring of blood flow and oxygenation in human breast cancer during early stages of neoadjuvant chemotherapy. *J Biomed Opt* 2007;12:3543-52.
  19. Yu G, Durduran T, Zhou C, et al. Noninvasive monitoring of murine tumor blood flow during and after photodynamic therapy provides early assessment of therapeutic efficacy. *Clin Cancer Res* 2005;11:3543-52.
  20. Yazdanfar S, Kulkarni MD, Izatt JA. High resolution imaging of *in vivo* cardiac dynamics using color Doppler optical coherence tomography. *Optics Exp* 1997;1:424-31.
  21. Chen Z, Milner TE, Dave D, Nelson JS. Optical Doppler tomographic imaging of fluid flow velocity in highly scattering media. *Optics Lett* 1997;22:64-6.
  22. Huang D, Swanson EA, Lin CP, et al. Optical coherence tomography. *Science* 1991;254:1178-81.
  23. Yazdanfar S, Rollins AM, Izatt JA. Imaging and velocimetry of the human retinal circulation with color Doppler optical coherence tomography. *Optics Lett* 2000;25:1448-50.
  24. Vakoc BJ, Yun SH, De Boer JF, Tearney GJ, Bouma BE. Phase-resolved optical frequency domain imaging. *Opt Exp* 2005;13:5483-93.
  25. Schaefer AW, Reynolds JJ, Marks DL, Boppart SA. Real-time digital signal processing-based optical coherence tomography and doppler optical coherence tomography. *IEEE Transact Biomed Eng* 2004; 51:186-90.
  26. Zhao Y, Chen Z, Saxer C, Xiang S, De Boer JF, Nelson JS. Phase-resolved optical coherence tomography and optical Doppler tomography for imaging blood flow in human skin with fast scanning speed and high velocity sensitivity. *Opt Lett* 2000;25:114-6.
  27. Yang VXD, Tang SJ, Gordon ML, et al. Endoscopic Doppler optical coherence tomography in the human GI tract: initial experience. *Gastrointest Endosc* 2005;61: 879-90.
  28. Cense B, Chen TC, Nassif N, et al. Ultra-high speed and ultra-high resolution spectral-domain optical coherence tomography and optical Doppler tomography in ophthalmology. *Bull Société Belge d'Ophtalmologie* 2006;302:123-32.
  29. Skliarenko JV, Lunt SJ, Gordon ML, Vitkin A, Milosevic M, Hill RP. Effects of the vascular disrupting agent ZD6126 on interstitial fluid pressure and cell survival in tumors. *Cancer Res* 2006;66:2074-80.
  30. Chen Z, Milner TE, Wang X, Srinivas S, Nelson JS. Optical Doppler tomography: imaging *in vivo* blood flow dynamics following pharmacological intervention and photodynamic therapy. *Photochem Photobiol* 1998;67: 56-60.
  31. Aalders MCG, Triesscheijn M, Ruevekamp M, et al. Doppler optical coherence tomography to monitor the effect of photodynamic therapy on tissue morphology and perfusion. *J Biomed Opt* 2006;11:044011.
  32. Standish BA, Yang VXD, Munce NR, et al. Doppler optical coherence tomography monitoring of microvascular tissue response during photodynamic therapy in an animal model of Barrett's esophagus. *Gastrointest Endosc* 2007;66:326-33.
  33. Collins HAKM, Moriyama ED, Mariampillai A, Dahlstedt E, Balaz R, Kuimova MK. Blood-vessel closure using photosensitizers engineered for two-photon excitation. *Nat Photon* 2008;2:420-4.
  34. Li H, Standish BA, Mariampillai A, et al. Feasibility of interstitial doppler optical coherence tomography for *in vivo* detection of microvascular changes during photodynamic therapy. *Lasers Surg Med* 2006;38:754-61.
  35. Yang VXD, Gordon ML, Qi B, et al. High speed, wide velocity dynamic range Doppler optical coherence tomography (Part I): system design, signal processing, and performance. *Opt Exp* 2003;11:794-809.
  36. Yang VXD, Gordon ML, Mok A, et al. Improved phase-resolved optical Doppler tomography using the Kasai velocity estimator and histogram segmentation. *Opt Commun* 2002;208:209-14.
  37. Roy M, DaCosta RS, Weersink R, et al. Quantum dots as contrast agents for endoscopy: Mathematical modeling and experimental validation of the optimal excitation wavelength. *SPIE* 2007;8:644812.
  38. Dam JS, Dalgaard T, Fabricius PE, Andersson-Engels S. Multiple polynomial regression method for determination of biomedical optical properties from integrating sphere measurements. *Appl Opt* 2000;39: 1202-9.
  39. Wilson B. Measurements of tissue optical properties: Methods and theories. In: AJ Welch MvG, editor. *Optical-Thermal Response of Laser-Irradiated Tissue*. New York: Plenum Press; 1995. p. 233-305.
  40. Jacques SLWL. Monte Carlo Modeling of Light Transport in Tissues. In: Welch AJMvG, editor. *Optical-Thermal Response of Laser-Irradiated Tissue*. New York: Plenum Press; 1995. p. 73-99.
  41. Jacques SL. Simple optical theory for light dosimetry during PDT. *SPIE* 1992;1645:155-65.
  42. Busch TM, Wileyto EP, Emanuele MJ, et al. Photodynamic therapy creates fluence rate-dependent gradients in the intratumoral spatial distribution of oxygen. *Cancer Res* 2002;62:7273-9.
  43. Johansson A, Axelsson J, Andersson-Engels S, Swartling J. Realtime light dosimetry software tools for interstitial photodynamic therapy of the human prostate. *Med Phys* 2007;34:4309-21.
  44. Huang Z, Chen Q, Luck D, et al. Studies of a vascular-acting photosensitizer, Pd-bacteriopheophorbide (Tookad), in normal canine prostate and spontaneous canine prostate cancer. *Lasers Surg Med* 2005;36:390-7.
  45. Svensson T, Andersson-Engels S, Einarsdóttir M, Svanberg K. In vivo optical characterization of human prostate tissue using near-infrared time-resolved spectroscopy. *J Biomed Opt* 2007;12:014022.
  46. Zhu TC, Finlay JC, Hahn SM. Determination of the distribution of light, optical properties, drug concentration, and tissue oxygenation in-vivo in human prostate during motexafin lutetium-mediated photodynamic therapy. *J Photochem Photobiol B* 2005;79:231-41.
  47. Solonenko M, Cheung R, Busch TM, et al. *In vivo* reflectance measurement of optical properties, blood oxygenation and motexafin lutetium uptake in canine large bowels, kidneys and prostates. *Phys Med Biol* 2002; 47:857-73.
  48. Wang HW, Putt ME, Emanuele MJ, et al. Treatment-induced changes in tumor oxygenation predict photodynamic therapy outcome. *Cancer Res* 2004;64:7553-61.
  49. Kruijt B, De Bruijn HS, Van Der Ploeg - Van Den Heuvel A, Sterenberg HJCM, Robinson DJ. Laser speckle imaging of dynamic changes in flow during photodynamic therapy. *Lasers Med Sci* 2006;21:208-12.
  50. Ohlerth S, Luluhova D, Buchholz J, Roos M, Walt H, Kaser-Hotz B. Changes in vascularity and blood volume as a result of photodynamic therapy can be assessed with power Doppler ultrasonography. *Lasers Surg Med* 2006;38:229-34.
  51. Powers BE, Withrow SJ, Thrall DE, et al. Percent tumor necrosis as a predictor of treatment response in canine osteosarcoma. *Cancer* 1991;67:126-34.
  52. Leach RM, Hill HS, Snetkov VA, Ward JPT. Hypoxia, energy state and pulmonary vasomotor tone. *Respir Physiol Neurobiol* 2002;132:55-67.
  53. Khurana M, Moriyama EH, Mariampillai A, Wilson BC. Intravital high resolution optical imaging of individual vessel response to photodynamic treatment. *J Biomed Opt* 2008;13:040502.
  54. Mariampillai A, Standish BA, Moriyama EH, et al. Speckle Variance Detection of Microvasculature using Swept Source Optical Coherence Tomography. *Opt Lett* 2008;33:1530-2.
  55. Luo Y, Arauz LJ, Castillo JE, Barton JK, Kostuk RK. Parallel optical coherence tomography system. *Applied Opt* 2007;46:8291-7.
  56. Vakoc BJ, Shishko M, Yun SH, et al. Comprehensive esophageal microscopy by using optical frequency-domain imaging (with video). *Gastrointest Endosc* 2007;65:898-905.
  57. Wilson BC. Detection and treatment of dysplasia in Barrett's esophagus: A pivotal challenge in translating biophotonics from bench to bedside. *J Biomed Opt* 2007; 12:051401.